Nuclear Instruments and Methods in Physics Research A 810 (2016) 27–31

Contents lists available at ScienceDirect

Nuclear Instruments and Methods in Physics Research A

journal homepage: www.elsevier.com/locate/nima

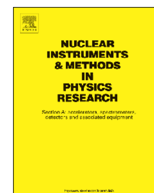

Fabrication of a thin silicon detector with excellent thickness uniformity

E. Valtonen [a,*], T. Eronen [a], S. Nenonen [b], H. Andersson [b], K. Miikkulainen [b], S. Eränen [c,1], H. Ronkainen [c], J. Mäkinen [d], H. Husu [e,2], A. Lassila [e], R. Punkkinen [f], M. Hirvonen [g]

[a] Department of Physics and Astronomy, University of Turku, FI-20014 Turku, Finland
[b] Oxford Instruments Analytical Oy, P.O. Box 85, FI-02631 Espoo, Finland
[c] VTT Technical Research Centre of Finland Ltd, P.O. Box 1000, FI-02044 VTT, Finland
[d] Okmetic Oyj, P.O. Box 44, 01301 Vantaa, Finland
[e] Centre for Metrology and Accreditation, P.O. Box 9, FI-02151 Espoo, Finland
[f] Department of Information Technology, University of Turku, FI-20014 Turku, Finland
[g] Aboa Space Research Oy, Tierankatu 4B, FI-20520 Turku, Finland

ARTICLE INFO

Article history:
Received 16 October 2015
Received in revised form
25 November 2015
Accepted 25 November 2015
Available online 2 December 2015

Keywords:
Silicon detector
SOI technology
Thickness uniformity
Fizeau interferometer
ΔE-E
Solar energetic particles

ABSTRACT

We have fabricated and tested a thin silicon detector with the specific goal of having a very good thickness uniformity. SOI technology was used in the detector fabrication. The detector was designed to be used as a ΔE detector in a silicon telescope for measuring solar energetic particles in space. The detector thickness was specified to be 20 μm with an rms thickness uniformity of ± 0.5%. The active area consists of three separate elements, a round centre area and two surrounding annular segments. A new method was developed for measuring the thickness uniformity based on a modified Fizeau interferometer. The thickness uniformity specification was well met with the measured rms thickness variation of 43 nm. The detector was electrically characterized by measuring the *I*–*V* and *C*–*V* curves and the performance was verified using a ^{241}Am alpha source.

© 2015 Elsevier B.V. All rights reserved.

1. Introduction

Thin silicon detectors have been extensively used in ΔE-E-telescopes in applications where nuclear particles have to be identified [1]. Such applications include isotope identification and energy measurement of fragments produced in nuclear collisions in physics experiments [2–6] and measurement of solar energetic particles and cosmic rays in space [7–9]. Thin detectors are required to identify high-Z particles and to minimize the energy threshold for detection. Thin silicon detectors are also used in measurements of short-range particles under high gamma ray background [10], as transmission detectors in single-ion irradiation experiments [11,12], and in characterization of the plasma environment in fusion experiments [13]. Application of thin silicon detectors for beam monitoring in high-intensity accelerator environments has been studied due to their higher radiation tolerance compared to thicker detectors [14,15]. Thin pixel detectors have been investigated for a precise measurement of particle tracks in experiments, where multiple scattering is a concern [16–18] or absorption of particles needs to be minimized [19].

Several methods can be employed for the fabrication of thin silicon detectors. In principle, a straightforward way is to use a starting wafer with appropriate thickness. Processing and handling of thin wafers would, however, be demanding. A common method has been to use a wafer with standard thickness (~300–400 μm) and etch the active area of the detector to the desired smaller thickness, which is achieved basically by controlling the etching time when the etch rate is known [3,11,12,14,20,21]. To control the etch stop and to improve the thickness uniformity, growth of an epitaxial layer on highly doped silicon has been successfully exploited [5,22]. A recognized disadvantage of epitaxial silicon has been its relatively high density of impurities and defects. Still another method is to use Silicon-On-Insulator (SOI) technology with a buried silicon oxide as the etch stop layer [10,13,16]. In this case, the detector thickness and its uniformity are precisely controlled by the characteristics of the thinned device layer.

In a ΔE-E telescope, the quality of the ΔE detector largely determines the performance of the instrument in particle

* Corresponding author.
E-mail address: eino.valtonen@utu.fi (E. Valtonen).
[1] Deceased.
[2] Current address: nLIGHT Corporation, Sorronrinne 9, 08500 Lohja, Finland.

http://dx.doi.org/10.1016/j.nima.2015.11.124
0168-9002/© 2015 Elsevier B.V. All rights reserved.

identification. In addition to the electrical characteristics of the detector, the energy loss fluctuations of charged particles passing through the detector define the energy resolution [2]. In thin detectors, variations in the sensitive thickness can have a significant contribution to the energy loss fluctuations.

We have used SOI technology to fabricate extremely uniform silicon detectors with a thickness of 20 μm. In the course of the work, we developed a new precise method for thickness uniformity measurement. The detector was developed for the Low Energy Telescope of the Energetic Particle Detector suite on Solar Orbiter for measuring species of solar energetic particle in the charge range 1–28 at energies above 1 MeV/nucleon.

In Sections 2 and 3 we describe the detector design and fabrication process, respectively. Detector characterization is briefly described in Section 4. The method and results of thickness uniformity measurements are discussed in Section 4.1. Electrical characterizations are summarized in Section 4.2 and in Section 4.3 we describe the basic performance of the detector as deduced from radioactive source tests. Conclusions are presented in Section 5.

2. Detector requirements

The detector was designed to be used as the first ΔE detector of a 5-element particle telescope for measuring solar energetic ions from hydrogen ($Z=1$) to nickel ($Z=28$) in space. The thickness of the detector was specified to be 20 μm as a trade-off between a low detection threshold and capability to still reliably detect 20 MeV protons having most probable energy loss of 95 keV in 20 μm silicon with ~30 keV FWHM statistical fluctuations. The total active area of the detector was fixed to 2.1 cm^2 (diameter 1.64 cm) in order to be able to record also low particle fluxes with a cadence of 10 s with sufficient statistical accuracy. Because high fluxes also had to be measured without significant saturation, the detector surface was divided into three independent parts: a central active area of 5.2 mm diameter and a surrounding annular area further divided into two equal segments (Fig. 1). The subdivision of the annular area allows the signal from the centre part to be connected to a bonding pad at the edge of the detector. A guard ring fully surrounds all the active areas, the centre signal lead, and the bonding pads. The detector is biased by using punch-through effect from a circular n^+-doped ring on the front surface.

Very good thickness uniformity was set as the primary goal of the detector development. The scientific performance requirement was to separate ^{3}He from ^{4}He down to the level of ~1% and to distinguish most abundant (even-Z) isotopes of elements up to magnesium. The thickness uniformity specification was set at ±0.5% (rms), i.e., ±0.1 μm (rms) for the 20 μm detector. In the telescope design, the field of view was limited to ±20° relative to normal incidence for the entire detector and to ±7° for the central part by using equally subdivided detector (80 μm thick) below the first ΔE detector. The requirement for typical leakage current at full depletion was 2 nA/cm^2 (maximum 5 nA/cm^2) at 20 °C. The main electronic noise component in the detector signal was expected to result from the capacitive load caused by the detector at the preamplifier input. The subdivision of the detector active area in three parts reduces this noise contribution.

3. Fabrication process

3.1. SOI wafer production

The detector prototypes described here were fabricated by using the SOI (Silicon-On-Insulator) technology. In this technique, the active sensor wafer is bonded to a carrier or handle wafer, after which the sensor wafer is thinned down to a required thickness. *N*-type high resistivity, >5 kΩ cm, 150 mm diameter single side polished wafers from Topsil Semiconductor Materials A/S (Denmark) were used as sensor wafers. The thickness of the wafers was 665-685 μm and their orientation was ⟨100⟩. The handle wafers were *p*-type boron doped Czochralski-grown double side polished 150 mm wafers from Okmetic Oyj (Finland). The thickness of the wafers was 380 μm with a resistivity of 1–5 Ω · cm and orientation of ⟨100⟩.

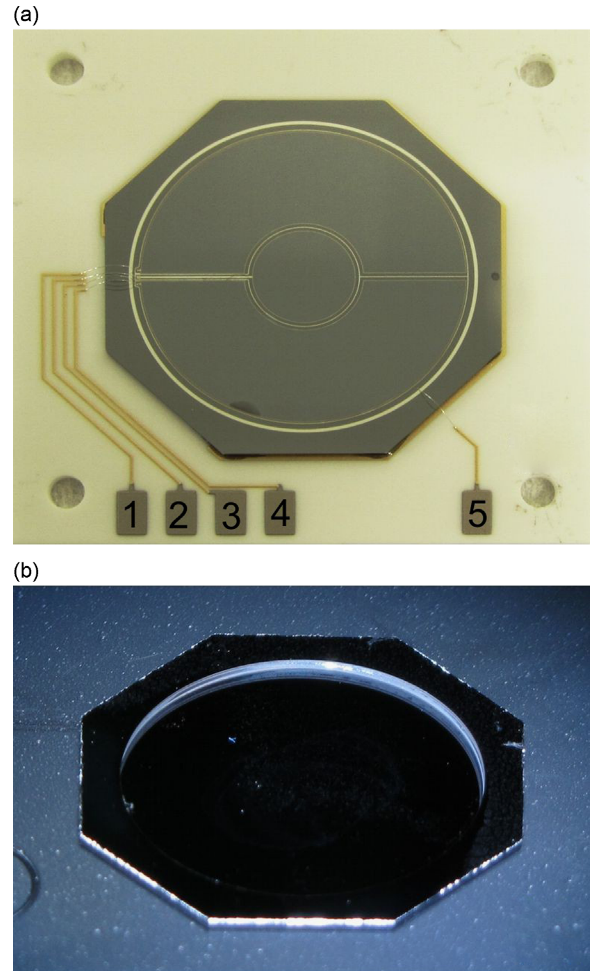

Fig. 1. (a) Photograph of the detector front side showing the division of active areas. The detector chip is glued and wire-bonded onto a ceramic substrate. The contact pads shown in the figure are (1) upper detector segment, (2) centre detector, (3) guard ring, (4) lower detector segment, and (5) bias (n^+). All contact pads on the detector are outside the membrane area. (b) The thinned back side of the detector demonstrating the good quality of the etching process at the edge of the active area.

The sensor and handle wafers were bonded together by using a special low temperature bonding process at VTT. First, 43.5 nm thick silicon oxide layer was grown on the sensor wafer, then the back side (the side to be bonded) of the sensor wafer was implanted with As (10^{15} cm^{-2}, 120 keV), after which the oxide was removed. Then a 488 nm thick oxide layer was grown on the handle wafer. The wafers were rinsed with de-ionized water and spinned dry in a rinse/dryer. Before the bonding, the wafer surfaces were plasma activated in Aviza ICP etcher. The activated surfaces were then vacuum bonded together in wafer bonder EVG 5210S. The bonding was finalized in a nitrogen atmosphere in an annealing furnace at 425 °C for 2 h. After the bonding, the sensor wafer was thinned down to 20 μm first by grinding and then by Chemical Mechanical Polishing (CMP) at Okmetic.

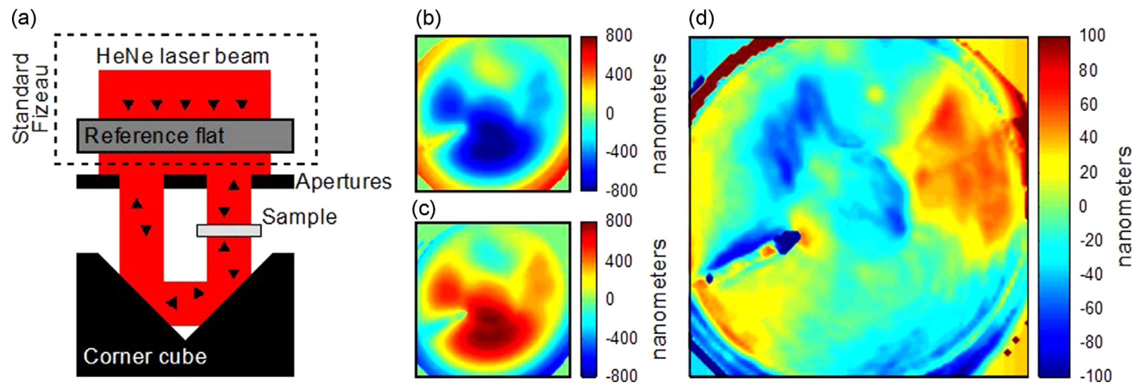

Fig. 2. (a) Schematic image of the setup for measuring the uniformity of the detector thickness. The measured profiles of (b) top and (c) bottom surfaces. (d) The corrected thickness uniformity profile of the sample.

3.2. Detector processing

The detector processing was started by growing a 50 nm thick thermal oxide layer (dry 1000 °C, 60 min) on the front side of the sensor wafer, forming the field oxide. This was followed by boron implantation of the entrance window section and guard ring areas. The implantation was made very shallow by using low ion energy, 10 keV, and low dose, $5\cdot10^{13}$ cm^{-2}. Then the biasing ring area, around the entrance window region, was ion implanted with phosphorus, 100 keV, 10^{15} cm^{-2}. Next, the wafers were annealed in a nitrogen atmosphere at 700 °C for 30 min. Based on our previous experience, this relatively low temperature is sufficient for n^+ annealing.

The contact openings to the ion implanted regions were etched at the edges (periphery) of the entrance window sections and above the ion-implanted guard ring and bias ring areas. The contact openings were then covered with a 500 nm thick sputtered aluminium layer. To avoid a long bond-wire, a metal line connects the centre diode to the bonding pad at the edge. The metal line was formed on top of the field oxide to minimize its capacitance.

Finally, the handle wafer material was removed from the entrance window region by using the *Aviza* deep Si etching system at VTT. The oxide layer (of the handle wafer) between the sensor wafer and handle wafer, so-called buried oxide, acted as an etch stopping layer. As a result, a cavity was formed, revealing a free-standing 20 µm thick membrane. The remaining handle wafer material around the cavity acts as a support structure for the membrane.

The thickness of the dead layers on both sides of the detector was estimated to be simply the sum of the thicknesses of the oxide layer and the implanted layer. The total dead layer on the front side of the detector consists of 50 nm thick SiO_2 layer and the boron implanted p^+ layer, which was estimated to be 150–200 nm thick. Similarly, the total thickness of the dead layer on the back side consists of the arsenic-doped n^+ layer and the 165 nm thick SiO_2 layer. The depth profiles of the implantations after annealing were simulated by using the ICECREM software [23].

4. Detector characterization

4.1. Mechanical characterization

Thin detectors may suffer from both microscopic inhomogeneities and macroscopic thickness variations. The former may arise from surface roughness, which is not removed during the fabrication process. Macroscopic thickness variations refer to the change of thickness of the detector over the large active area. Both these defects are minimized when using SOI technology.

After the thinning, the thickness of the sensor wafers was measured at nine different locations on the wafer for seven bonded wafers by using FTIR (Fourier Transform Infrared Spectroscopy) at Okmetic. In the best case, the difference between the measured maximum and minimum thicknesses for the wafer was 170 nm and the standard deviation was 54 nm. In the worst case, the corresponding values for the wafer were 340 nm and 115 nm.

The uniformity of the detector thickness after processing was measured with a modified Fizeau interferometer with a Helium-Neon laser (wavelength 632.8 nm) as a light source. A standard Fizeau interferometer measures optical flatness of a surface. The interferometer was calibrated with a three-flat test, which is an error separation method. In the developed measurement, a corner cube was placed below the sample to direct part of the laser beam to the bottom surface of the sample (Fig. 2(a)). The top surface was measured normally. This configuration allows simultaneous measurement of both surfaces. The interference occurs between the fields reflected from the sample top/bottom surface and the bottom surface of the reference flat. A block with two apertures is used to illuminate only the desired sample areas on the top and bottom surfaces.

The topographic profiles of the top and bottom surfaces are shown in Fig. 2(b) and (c), respectively. The thickness variation of the film was obtained as a difference of the top and bottom surface profiles, which require careful lateral adjustment to properly overlap the profiles. The flatness deviation of the transmitted wavefront of the corner cube was measured with the same Fizeau interferometer and the maximum deviation was about 75 nm peak-to-peak. The linear part of the error is the dominating contribution, and thus a linear fit was applied to the error data, and furthermore the linearized error was removed from the measured thickness variation profile. The corrected thickness uniformity profile is shown in Fig. 2(d) with a maximum thickness variation of about 150 nm and rms thickness variation of 43 nm. The total expanded uncertainty ($k=2$) of the measurement is estimated to be about 50 nm.

4.2. Electrical characterization

I–V and *C–V* characterization was done for a number of detectors. All measurements were done at the temperature of 20.0 ± 0.5 °C. In *C–V* measurements a frequency of 100 kHz was used. Examples of the detector leakage currents as a function of reverse voltage are shown in Fig. 3. Capacitance measurements (see Fig. 4) indicate that the detector reaches full depletion already at the reverse voltage of >-1 V. The requirement was that the leakage current at full depletion is at maximum 5 nA/cm^2 (typically 2 nA/cm^2), which was achieved. However, with increasing absolute value of the reverse voltage the leakage current does not

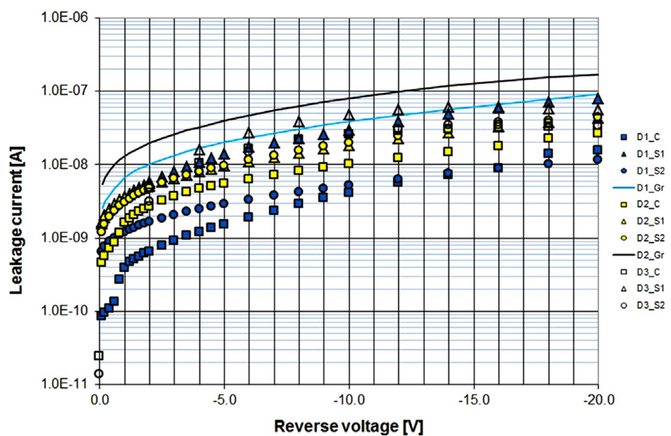

Fig. 3. Leakage currents as function of reverse voltage for three detectors. C stands for the centre active area and S1 and S2 for the side segments. Note that in this scale many of the D3 centre and segment 2 points are masked by those of the D2 segments 1 and 2.

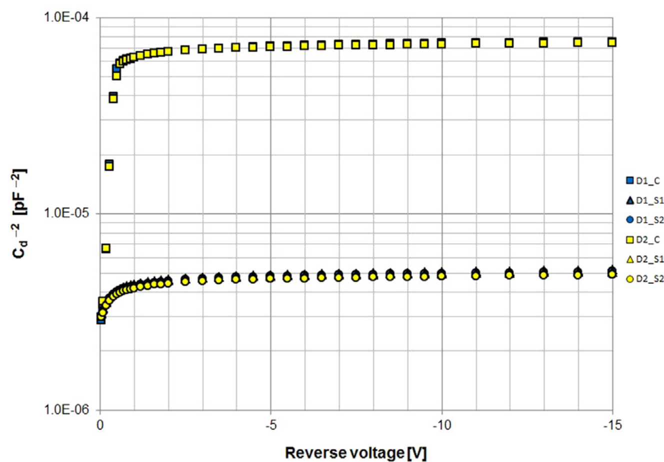

Fig. 4. Inverse square of the detector capacitance as function of reverse voltage for the three active areas of two sample detectors. The capacitances of the centre active areas and the side segments, respectively, of these two detectors were essentially the same.

fully level off, but keeps growing, and already at an operating voltage of −5 V would be outside the preferred value. We believe that the excess leakage current is caused by a non-optimal guard ring layout, too sharp corners, etc. The contribution of the leakage current to the total electronic noise is, however, still acceptable as the major part of the noise is caused by the high capacitance of the detector. As seen in Fig. 3, the leakage current of the guard ring reaches values of several tens to hundred nanoamps, and in the case of detector D3 (not shown in Fig. 3) exceeds 1 μA.

The measured capacitances of the centre active areas at −5 V reverse voltage (full depletion) were found to be ~120 pF and those of the side segments were found to be ~455 pF. The inverse squares of the detector capacitances are shown for two detectors as a function of reverse voltage in Fig. 4. From this figure, the absolute value of the full depletion voltage of less than 1 V can be obtained.

4.3. Detector performance

Performance tests of the detector were carried out by using a ^{241}Am alpha source. The source was uncollimated and was at a distance of 25 mm from the detector. The source and the detector were placed in a vacuum chamber and the detector was connected to a charge-sensitive preamplifier (Tennelec TC101) outside of the

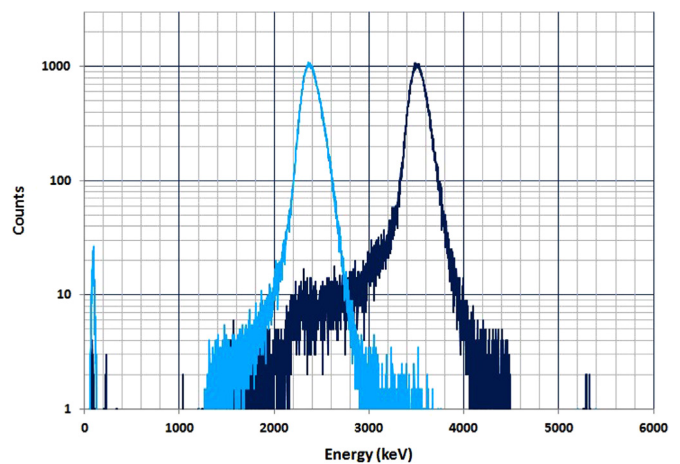

Fig. 5. Response of the 20 μm (nominal thickness) SOI detector to 5.486 MeV alpha particles (right) compared to the response of a 15.3 μm surface barrier detector (left). The measurements were done separately and independently from each other, but are here plotted in the same figure with the same energy scale.

chamber with a coaxial cable with a length of about 20 cm. The preamplifier signal was further amplified and shaped with a spectroscopy amplifier (EG&G Ortec 672, $\tau = 3$ μs) and fed to the input of an analog-to-digital converter (Silena 4418/V). The timing output of the preamplifier was used to create the gate for the AD-converter. Measurements were done by using various bias voltages between −3 V and −12 V. No significant differences were found in the results with different operating voltages. The average FWHM energy resolution of 5.486 MeV alpha particles was found to be 4.9% for the centre active area and 5.8% for the side segments. An example of the measured pulse height distributions for the centre active area of the detector is shown in Fig. 5. For comparison is shown the ^{241}Am alpha spectrum measured with an EG&G Ortec surface barrier detector. For this detector, the manufacturer had specified a thickness of 15.3 μm based on a 5-point thickness measurement. The active area of the detector was 100 mm^2. For this thinner detector, an energy resolution of 6.6% was obtained. The SOI detector shows rather high low-energy tail in the spectrum. One reason for this could be the uncollimated source causing α-particles to hit the edges of the small active area and losing charge to the surrounding guard ring. Cross talk from the surrounding segments is also possible, but is considered less probable due to the guard ring between the diode elements.

Measurements were also done in a coincidence arrangement using a fabricated 20 μm detector as the transmission (ΔE) detector and a standard 50 mm^2 300 μm thick Canberra ion-implanted planar detector as the stopping (residual E) detector. In this case, the AD-converter gate was created by coincident signals from the two silicon detectors. Results are shown in Fig. 6. The coincidence measurement proved to provide a very sensitive and accurate method for determining the absolute thickness of the ΔE detector by comparing theoretical energy losses in both detectors. The sensitivity of the method follows from the fact that when changing the thickness of the ΔE detector, the most probable energy losses in the two detectors move in opposite directions. Fig. 6 also shows simulated pulse height spectra. The simulations were carried out by using the multi-layer shielding simulation software (Mulassis) of the Spenvis system [24]. The current version of Mulassis (V 1.23) uses the Geant4 toolkit (Version 9.5p02) to simulate radiation transport through a user-defined geometry. The simulation results shown in Fig. 6 were obtained for a ΔE detector with an active layer thickness of 20.02 μm and with the dead layer thicknesses of 50 nm (SiO_2) and 200 nm (p^+, Si) in the front side, and 100 nm (n^+, Si) and 165 nm

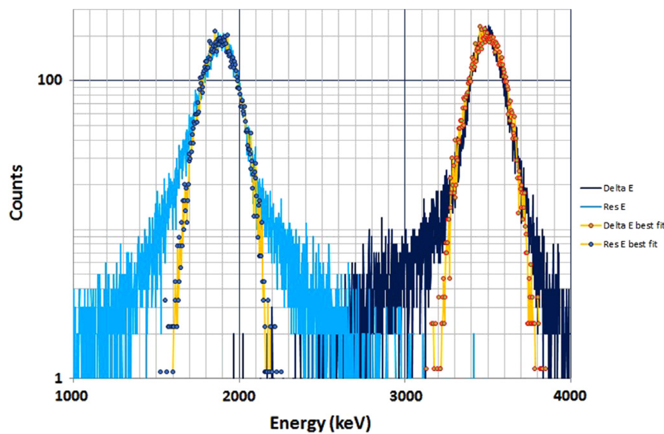

Fig. 6. Energy losses of 5.486 MeV alpha particles in the 20 μm (nominal thickness) SOI ΔE detector (right) and in a 300 μm residual energy detector (left). Distributions of coincident signals from the two detectors are presented. Also shown are the simulation results of energy losses with actual detector and dead layer thicknesses as given in the text.

(SiO_2) on the back side of the detector. The thickness 20.02 μm of the ΔE detector agrees well with the FTIR measurements of the sensor wafer after the thinning process (see Section 4.1). The sensitivity of the method can be judged from the fact that already a change of 50 nm in the ΔE detector or the dead layer thickness leads to significantly different most probable energy losses in the ΔE and residual energy detectors, which can be compared with experimental results.

5. Conclusions

We have designed, fabricated, and characterized a thin 3-element silicon detector with excellent thickness uniformity. The design goal for the uniformity was ±0.5% (rms) for the 20 μm thick detector. Thickness uniformity measurement of a test sample showed an rms thickness variation of 43 nm over the surface of the detector. This excellent result was obtained by using the SOI technology. The detector was electrically characterized by measuring the *I–V* and *C–V* curves. The performance was tested by using a ^{241}Am alpha source. The FWHM energy resolution was found to be 4.9% for the centre active region (~21 mm^2) and 5.8% for the side segments (~95 mm^2). Using a coincidence measurement, the absolute thickness of a test sample was found to be 20.02 μm by comparing the measured results with GEANT-4 based simulations.

Acknowledgements

We acknowledge support by the Finnish Funding Agency for Innovation (Tekes) under Grant 40176/11.

References

[1] F.S. Goulding, B.G. Harvey, Annual Review of Nuclear and Particle Science 25 (1975) 167.
[2] A.G. Seamster, R.E.L. Green, R.G. Korteling, Nuclear Instruments and Methods in Physics Research 145 (1977) 583, http://dx.doi.org/10.1016/0029-554X(77)90590-0.
[3] L. Lavergne-Gosselin, L. Stab, M.O. Lampert, H.-Å Gustafsson, B. Jakobsson, A. Kristiansson, A. Oskarsson, M. Westenius, A.J. Kordyasz, K. Aleklett, L. Westerberg, M. Rydehell, O. Tengblad, Nuclear Instruments and Methods in Physics Research A 276 (1989) 210, http://dx.doi.org/10.1016/0168-9002(89)90634-7.
[4] P. Golubev, V. Avdeichikov, L. Carlén, B. Jakobsson, A. Siwek, E.J. van Veldhuizen, L. Westerberg, H.J. Whitlow, Nuclear Instruments and Methods in Physics Research A 500 (2003) 96, http://dx.doi.org/10.1016/S0168-9002(03)00302-4.
[5] A.J. Kordyasz, M. Kowalczyk, E. Nossarzewska-Orłowska, M. Kisieliński, E. Kulczycka, J. Sarnecki, J. Iwanicki, Nuclear Instruments and Methods in Physics Research A 570 (2007) 336, http://dx.doi.org/10.1016/j.nima.2006.09.063.
[6] A.J. Kordyasz, N. Le Neindre, M. Parlog, G. Casini, R. Bougault, G. Poggi, A. Bednarek, M. Kowalczyk, O. Lopez, Y. Merrer, E. Vient, J.D. Frankland, E. Bonnet, A. Chbihi, D. Gruyer, B. Borderie, G. Ademard, P. Edelbruck, M.F. Rivet, F. Salomon, M. Bini, S. Valdré, E. Scarlini, G. Pasquali, G. Pastore, S. Piantelli, A. Stefanini, A. Olmi, S. Barlini, A. Boiano, E. Rosato, A. Meoli, A. Ordine, G. Spadaccini, G. Tortone, M. Vigilante, E. Vanzanella, M. Bruno, S. Serra, L. Morelli, M. Guerzoni, R. Alba, D. Santonocito, C. Maiolino, M. Cinausero, F. Gramegna, T. Marchi, T. Kozik, Kulig P., T. Twaróg, Z. Sosin, Gasior K., A. Grzeszczuk, W. Zipper, J. Sarnecki, D. Lipiński, H. Wodzińska, A. Brzozowski, M. Teodorczyk, M. Gajewski, A. Zagojski, K. Krzyżak, K.J. Tarasiuk, Z. Khabanowa, L. Kordyasz, European Physical Journal A 51 (2015) 15, http://dx.doi.org/10.1140/epja/i2015-15015-2.
[7] D.E. Stilwell, W.D. Davis, R.M. Joyce, F.B. McDonald, J.H. Trainor, W.E. Althouse, A.C. Cummings, T.L. Garrard, E.C. Stone, R.E. Vogt, IEEE Transactions on Nuclear Science NS-26 (1979) 513, http://dx.doi.org/10.1109/TNS.1979.4329683.
[8] E. Valtonen, J. Peltonen, P. Peltonen, T. Eronen, E. Hoisko, M. Louhola, M. Lumme, A. Nieminen, E. Riihonen, M. Teittinen, J. Torsti, K. Ahola, C. Holmlund, V. Kelhä, K. Leppälä, P. Ruuska, E. Strömmer, R. Verkasalo, E. Koivula, M. Moilanen, Nuclear Instruments and Methods in Physics Research A 391 (1997) 249, http://dx.doi.org/10.1016/S0168-9002(97)00469-5.
[9] R.A. Mewaldt, C.M.S. Cohen, W.R. Cook, A.C. Cummings, A.J. Davis, S. Geier, B. Kecman, J. Klemic, A.W. Labrador, R.A. Leske, H. Miyasaka, V. Nguyen, R.C. Ogliore, E.C. Stone, R.G. Radocinski, M.E. Wiedenbeck, J. Hawk, S. Shuman, T.T. von Rosenvinge, K. Wortman, Space Science Reviews 136 (2008) 285, http://dx.doi.org/10.1007/s11214-007-9288-x.
[10] F. Foulon, L. Rousseau, L. Babadjian, S. Spirkovitch, A. Brambilla, P. Bergonzo, IEEE Transactions on Nuclear Science NS-46 (1999) 218, http://dx.doi.org/10.1109/23.775517.
[11] G. Thungström, L. Westerberg, R. Spohr, C. Sture Petersson, Nuclear Instruments and Methods in Physics Research A 546 (2005) 312, http://dx.doi.org/10.1016/j.nima.2005.03.053.
[12] N. Abdel, J. Pallon, M. Graczyk, I. Maximov, L. Wallman, IEEE Transactions on Nuclear Science NS-60 (2013) 1182, http://dx.doi.org/10.1109/TNS.2012.2230644.
[13] J. Kalliopuska, F. García, M. Santala, S. Eränen, S. Karttunen, T. Virolainen, T. Kovero, T. Vehmas, R. Orava, Nuclear Instruments and Methods in Physics Research A 591 (2008) 92, http://dx.doi.org/10.1016/j.nima.2008.03.030.
[14] S. Ronchin, M. Boscardin, G.-F. Dalla Betta, P. Gregori, V. Guarnieri, C. Piemonte, N. Zorzi, Nuclear Instruments and Methods in Physics Research A 530 (2004) 134, http://dx.doi.org/10.1016/j.nima.2004.05.061.
[15] E. Fretwurst, L. Andricek, F. Hönniger, G. Kramberger, G. Lindström, G. Lutz, M. Reiche, R.H. Richter, A. Schramm, Nuclear Instruments and Methods in Physics Research A 552 (2005) 124, http://dx.doi.org/10.1016/j.nima.2005.06.019.
[16] L. Andricek, G. Lutz, M. Reiche, R.H. Richter, IEEE Transactions on Nuclear Science NS-51 (2004) 1117, http://dx.doi.org/10.1109/TNS.2004.829531.
[17] D. Calvo, P. De Remigis, T. Kugathasan, G. Mazza, A. Rivetti, R. Wheadon, Nuclear Instruments and Methods in Physics Research A 624 (2010) 290, http://dx.doi.org/10.1016/j.nima.2010.04.149.
[18] M. Battaglia, D. Contarato, P. Denes, D. Liko, S. Mattiazzo, D. Pantano, Nuclear Instruments and Methods in Physics Research A 681 (2012) 61, http://dx.doi.org/10.1016/j.nima.2012.04.043 arXiv:1204.2910.
[19] P. Riedler, J. Rochet, A. Rudge, M. Doser, R. Landua, Nuclear Instruments and Methods in Physics Research A 478 (2002) 316, http://dx.doi.org/10.1016/S0168-9002(01)01817-4.
[20] L. Evensen, T. Westgaard, V. Avdeichikov, L. Carlen, B. Jakobsson, Y. Murin, J. Martensson, A. Oskarsson, A. Siwek, E.J. van Veldhuizen, L. Westerberg, M. Guttormsen, H.J. Whitlow, IEEE Transactions on Nuclear Science NS-44 (1997) 629, http://dx.doi.org/10.1109/23.603723.
[21] S. Ma, Y. Li, L. Zhang, J. Wang, Y. Jin, Journal of Instrumentation 5 (2010) 9005, http://dx.doi.org/10.1088/1748-0221/5/09/P09005.
[22] L. Stab, Nuclear Instruments and Methods in Physics Research A 288 (1990) 24, http://dx.doi.org/10.1016/0168-9002(90)90458-I.
[23] P. Pichler, R. Dürr, N. Holzer, K. Schott, A. Barthel, J. Lorenz, H. Ryssel, Software Forum Digest (1989) 173.
[24] 〈https://www.spenvis.oma.be/〉.